https://doi.org/10.1016/j.ijhydene.2020.02.169

Thermal Effects in H_2O and CO_2 Assisted Direct Carbon Solid Oxide Fuel Cells

Qijiao He [a], Jie Yu [a], Haoran Xu[a], Dongqi Zhao [a,b], Tianshou Zhao [c] *, Meng Ni [a] *

a. *Building Energy Research Group, Department of Building and Real Estate, The Hong Kong Polytechnic University, Hung Hom, Kowloon, Hong Kong.*
b. *School of Artificial Intelligence and Automation, Key Laboratory of Image Processing and Intelligent Control of Education Ministry, Huazhong University of Science and Technology, Wuhan, Hubei, China.*
c. *HKUST Energy Institute, Department of Mechanical and Aerospace Engineering, The Hong Kong University of Science and Technology, Clear Water Bay, Kowloon, Hong Kong.*

∗ Corresponding author: T.S. Zhao and M. Ni.
E-mail address: metzhao@ust.hk (T.S. Zhao), meng.ni@polyu.edu.hk (M. Ni)

Abstract

Thermal effects in a H_2O and CO_2 assisted tubular direct carbon solid oxide fuel cell (DC-SOFC) are numerically investigated. Parametric simulations are further conducted to study the effects of operating potential, the distance between carbon and anode, inlet gas temperature, and anode inlet gas flow rate on the thermal behaviors of the fuel cell. It is found that the fuel cell with H_2O as gasification agent performs considerably better than the cell with CO_2 as gasification agent in all cases. It is also found that the temperature field of the fuel cell is highly uneven. The breakdown of the heat sources in the fuel cell shows that the H_2O assisted DC-SOFC has much higher heat generation and consumption than the CO_2 assisted cell. Interestingly, a thermal neutral voltage is observed, at which no heating or cooling of the cell is needed. In addition, the distance between the anode and the carbon layer is required to be as small as possible, which improvees the temperature uniformity of the fuel cell. The results of this study demonstrates the importance of thermal effects in DC-SOFCs and form a solid foundation for DC-SOFC thermal management.

Key words: Direct carbon solid oxide fuel cell (DC-SOFC); Thermal effect; Gasification agent; Numerical modeling; Temperature distribution.

Nomenclature

B_0	permeability of the porous electrodes, m^2
c	specific heat capacity, J kg^{-1} K^{-1}
C_p	fluid thermal capacity, J K^{-1}
D_i	diffusion coefficient of component i, m^2 s^{-1}
E_{eq}	equilibrium potential, V
F	Faraday constant, 96485 C mol^{-1}
i	current density, A m^{-2}
i_0	exchange current density, A m^{-2}
n	number of electrons transferred
N_i	mass transport rate, kg m^{-3} s^{-1}
P	(partial) pressure, Pa
Q	heat source term
T	temperature, K
U	velocity, [m/s]
y_i	molar fraction of component i

Greek symbols

α	charge transfer coefficient
ε	porosity
k	permeability, m^2
$\eta_{act/ohmic}$	activation/ohmic overpotential, V
λ	thermal conductivity, W m^{-1} K^{-1}
μ	gas dynamic viscosity of fluid, N m^{-1} s^{-1}
ρ	density, kg m^{-3}
τ	tortuosity factor

Superscripts

0	standard or parameter at equilibrium conditions
eff	effective
l	local

Abbreviations

DC-SOFC	direct-carbon solid oxide fuel cell
Exp	experimental measurement
IC-SOFC	indirect-carbon solid oxide fuel cell
LSCF	lanthanum strontium cobalt ferrite
SCCM	standard cubic centime per minute
SDC	samarium-doped CeO2
Sim	numerical simulation
WGSR	water gas shift reaction
YSZ	yttrium stabilized zirconium

1. Introduction

The growing concern of the whole human society to environmental problems and energy crisis has promoted the worldwide research on clean and efficient energy technologies [1-3]. Although renewable wind and solar energy will play more and more pivotal role in energy supply, the main energy sources will continue to be fossil fuels in the coming decades [4]. Conventional technologies for power generation from fossil fuels are based on heat engines, which not only cause pollutant emissions including SO_x, CO_2, and NO_x, but also low energy conversion efficiency (30~40%) [5]. Therefore, advanced energy conversion technologies with higher efficiency and lower emission are urgently needed to more efficiently and cleanly convert fossil fuels into electrical power.

As one of the most competitive clean and highly efficient devices to convert fuels to electricity, solid oxide fuel cell (SOFC) has received rising interest [6-10]. A typical SOFC has a sandwiched structure, including a dense electrolyte in the middle for O^{2-} ions transportation and two side porous electrodes for electrochemical reactions. Unlike conventional power plants based on thermodynamic cycles involving combustion process, through electrochemical reactions, the chemical energy of fuels can be converted into power by SOFCs. As the energy conversion process in SOFCs is not a thermodynamic cycle, the Carnot cycle efficiency does not limit the energy efficiency. The energy efficiency of SOFCs can be higher than 50%, which is significantly higher than that of a coal-fired power plant. In addition, the dense electrolyte of SOFCs can separate the emission gases and make the emission control and post treatment easier. Therefore, SOFCs are promising to replace conventional power plants. Compared with other types of fuel cells requiring pure H_2 as fuel, such as proton exchange membrane fuel cells (PEMFCs), SOFCs are very fuel flexible as various alternative fuels can be used for power generation, including H_2, CO, methane, biogas, ethanol, NH_3, and solid carbon.

To achieve a higher energy density and lower overall cost, solid fuels are more attractive than gaseous fuels. The direct carbon solid oxide fuel cells (DC-SOFCs) have been developed in order to utilize the solid carbon in SOFCs directly. As solid carbon particles are much bigger than the pore size of the porous anode, the carbon fuel cannot enter the porous anode layer to be electrochemically oxidized. The solid carbon fuel needs to be gasified by H_2O or CO_2 to form gaseous fuels (e.g. CO and H_2), which are electrochemically oxidized for power generation. At the cathode side, air is supplied to the cathode chamber. O_2 molecules are conveyed through the porous cathode to the triple phase boundary (TPB) and are reduced (combined with electrons) to oxygen ions (O^{2-}). The produced oxygen ions (O^{2-}) are conveyed through the dense electrolyte to the anode side for oxidizing the gaseous fuels (e.g. CO and H_2)

and producing electrons.

Most of DC-SOFCs employ CO_2 for carbon gasification ($C + CO_2 = 2CO$), which is termed as reversible Boudouard reaction. Nakagawa et al. [11] firstly tested high-temperature DC-SOFC with CO fuel from gasification of charcoal. They proposed that the CO was electrochemically oxidized at the anode of DC-SOFC. Liu et al. [12] developed a novel tubular DC-SOFC which firstly used carbon black as fuel. In their preliminary examination, the DC-SOFC delivered a maximum power density of 104 mW cm^{-2} at 1123K. A DC-SOFC 3-cell-stack by Bai et al. [13] achieved a peak power output of 2.4 W and a volumetric power density of 700 mW cm^{-3} at 1123K. All these experimental results demonstrate the feasibility of DC-SOFCs for power generation from carbon. However, the DC-SOFs need to be operated at a high temperature (i.e. 1123K) due to the slow reversible Boudouard reaction for carbon gasification by CO_2. In order to enhance the Boudouard reaction to facilitate CO generation from carbon, various catalysts have been developed for the Boudouard reaction. Wu et al. [14] enhanced carbon gasification reaction rate by adopting Fe_mO_n-M_xO (M = Li, K, Ca) for catalyzing the Boudouard reaction in the DC-SOFC and attained a maximum power density of 297 mW cm^{-2} at 1123K, which was only slightly lower than that achieved using gaseous H_2 as fuel. In a study conducted by Jiao et al. [15], they used alkali to treat the coal char and found its specific surface area was enlarged so that the Boudouard reaction rate and the power output were consequently improved. The peak power density reached 220 mW cm^{-2} at 1123K for modified coal char, which was much higher than 62 mW cm^{-2} for conventional coal char. Wu et al. [16] developed DC-SOFC using brown coal with abundant Ca element as fuel to achieve a maximum power density of 221 mW cm^{-2} at 1123K. M.Dudek et al. [17] used the direct ceramic inkjet printing technology to make cermetallic multi-component anode material for DC-SOFC. The Cu modified Ni YSZ anode showed a secondary catalytic effect of CO generation in the Boudouard reaction. Wang et al. [18] fabricated a DC-SOFC stack with 4-cells-in-series on a single yttrium-stabilized-zirconia electrolyte plate, which could deliver 8.6 W h at 1093K, discharging at 200 mA for 14 h. The above-mentioned studies on DC-SOFC with CO_2 as carbon gasification demonstrated the feasibility of this technology and the importance of the carbon gasification process. Although the use of catalyst for the Boudouard reaction can enhance the carbon gasification kinetics to some extent, it is still insufficient. As a result, the operating temperature can hardly be lowered than 1123K, which is too high for efficient and durable operation of DC-SOFC.

Some researchers tried to improve the efficiency of DC-SOFC through other ways. Guo et al. [19] employed dual chamber with all porous electrolyte structure to develop the DC-SOFC. They successfully controlled the needed oxygen at the anode side, which avoided coke

formation on the anode side. Wu et al. [20] developed a high performance DC-SOFC. The cell can achieve power densities of 188, 108 and 48 mWcm^{-2} at 873, 823, and 773K, respectively. In their experiments, Zhou et al. [21] found that CO-CO_2 counter diffusion affected the DC-SOFC performance significantly, which was closely related to the distance between carbon and anode. This counter diffusion was more important at lower temperature and higher current. Wang et al. [22] studied the effects of fuel treating temperature and discharge mode on the fuel utilization of DC-SOFC and found that higher fuel utilization can be achieved by higher coal temperature and constant resistance mode.

In recent years, it is found that the operating temperature of DC-SOFC can be lowered without sacrificing the performance by using H_2O to replace CO_2 for carbon gasification. Thermodynamic analyses conducted by Lee et al. [23] indicate little variation in the DC-SOFC efficiency or work output between the CO_2 and H_2O as gasification agents. However, their thermodynamic analyses totally neglected the effects of H_2O and CO_2 on the carbon gasification kinetics, thus their study could not truly reflect the effects of gasification agents on the performance of DC-SOFC. Ong and Ghoniem [24] developed a 1D membrane-electrode-assembly model to study the indirect-carbon solid oxide fuel cell (IC-SOFC) with carbon gasification by H_2O or CO_2 in an external gasifier. It was evident from the numerical study that between 973 K and 1023 K the IC-SOFC performed 3-5 times better with H_2O than CO_2 recycling. This modeling study provided a good foundation to clarify the difference between CO_2 dry gasification and H_2O steam gasification. Nevertheless, this 1D model does not consider the internal carbon gasification for DC-SOFC, which is highly coupled with electrochemical reactions and counter diffusion processes. Recently, Xu et al. [25,26] conducted modeling and experimental studies on H_2O and CO_2 assisted DC-SOFC with internal carbon gasification process. Due to a more rapid carbon gasification rate and the easier hydrogen electrochemical oxidation in the anode, the maximum power density was improved from 158 mW cm^{-2} in CO_2 case to 385 mW cm^{-2} in H_2O case at 1123 K. Moreover, the in situ steam carbon gasification reaction was observed significantly speeding up by adding Na_2CO_3 as catalyst, which can improve the performance of H_2O assisted DC-SOFC. However, the temperature field of DC-SOFC was assumed uniform and the thermal effect was not taken into consideration in these studies.

The complex gas transport, heat transfer and the electrochemical/chemical reactions are all highly coupled in DC-SOFC. The carbon gasification reaction kinetics and the electrochemical processes are all temperature-dependent. The temperature field/thermal effect have significant impact on the performance of DC-SOFC. In order to fill the research gap, the model developed in previous study [25] is extended to investigate the thermal effects on the

temperature distribution of DC-SOFC with both CO_2 and H_2O as carbon gasification agent.

2. Computational Setup

2.1. Description of Computational Model

Fig. 1 presents a schematic diagram of the CO_2 assisted DC-SOFC (CO_2 case) and H_2O assisted DC-SOFC (H_2O case). The 2D mathematical model is developed to simulate the heat transfer, ion/electron transport, mass/momentum transport and chemical/electrochemical reactions in the DC-SOFC. The anode chamber is filled with porous solid carbon, which is placed very close to the porous anode. The CO_2 or H_2O is supplied as the gasification agent at the inlet of the anode chamber to react with the solid carbon inside the whole anode chamber. The original model details have been reported in our previous work [25], which has been well validated. The assumptions made in ref. [25] are adopted in the present investigation. In the porous electrode, TPBs are distributed uniformly and the electronic/ionic conducting phases are continuous and homogeneous. All gases are assumed as ideal gases, and gas flow is laminar and incompressible.

Compared with the previous work, the geometry model is extended from button cell to tubular cell for practical application consideration. The electrochemical part of the cell has a length of 10mm, an inner diameter of 12mm and an outer diameter of 12.864mm. The modeled tubular cell uses Ni-YSZ (yttrium stabilized zirconium) composites as anode, bilayer YSZ/samarium-doped CeO_2 (SDC) electrolyte and LSCF (lanthanum strontium cobalt ferrite) as cathode. The thickness of the anode, electrolyte and cathode are 400μm, 8μm and 24μm, respectively. The distance between carbon and anode is 550μm. Over a certain operation period, the amount of carbon in the carbon chamber can be assumed to be constant. Thus the DC-SOFC is assumed to be under steady state operating conditions. Tables 1-2 list the material properties, including the ionic/electronic conductivity, porosity, anode volume fraction, TPB active area per unit volume (S_{TPB}), the thermal conductivity λ, specific heat capacity c, and density ρ, respectively. The thermal radiation is assumed to be negligible.

Table 1. Material electric properties [27-31]

Materials or Parameters	Expression or Value	Unit
Ionic conductivity		
YSZ	$3.34\times10^{4}e^{\frac{-10300}{T}}$	S m^{-1}
SDC	$\frac{100}{T}\times10^{5.48077+\frac{3792.53}{T}}$	S m^{-1}
LSCF	$\frac{100}{T}\times10^{2.51289+\frac{3036.75}{T}}$	S m^{-1}

Electronic conductivity		
Ni	$3.27\times10^{6}-1065.3T$	S m^{-1}
LSCF	$\frac{100}{T}\times10^{4.32576+\frac{1024.26}{T}}$	S m^{-1}
Porosity		
Anode	0.6	/
Cathode	0.2	/
Anode volume fraction		
Ni	0.6	/
YSZ	0.4	/
S_{TPB}		
Electrode tortuosity	3	/
Anode layer	2.14×10^{5}	m^{2} m^{-3}
Cathode layer	2.14×10^{5}	m^{2} m^{-3}

Table 2. Material thermodynamic properties [32-38]

Materials	λ (W m^{-1} K^{-1})	c (J kg^{-1} K^{-1})	ρ (kg m^{-3})
Carbon	1.59	887.5	1700
Ni-YSZ	6.23	390.0	6870
SDC	1.77	450.0	7120
YSZ	2.57	525.0	6086
LSCF	2.00	568.0	6360

2.2. The Reaction Model

2.2.1. Chemical reactions

For the traditional DC-SOFC, the Boudouard reaction ($C+CO_2 \leftrightarrow 2CO$) plays a major role because it produces CO for subsequent electrochemical reaction, where solid carbon is the energy source and CO acts as an energy carrier to transport chemical energy from solid carbon to anode TPB. By adding H_2O to DC-SOFC, the H_2O gasification reaction ($C+H_2O \leftrightarrow CO+H_2$) replaces the Boudouard reaction and becomes the main chemical-reaction in the anode chamber as H_2O gasification has a much higher reaction rate. The reaction rate of the Boudouard reaction and H_2O gasification reaction [39] are expressed in Eqns. (1-2).

$$r_{c\_co_2} = \frac{K_1 P_{co_2}}{1+K_2 P_{co}+K_3 P_{co_2}} \tag{1}$$

$$r_{c\_H_2O} = \frac{K_4 P_{H_2O}}{1+K_5 P_{H_2}+K_6 P_{H_2O}} \tag{2}$$

The widely used chemical reaction parameters are adopted and listed in Table 3.

Table 3. Chemical reaction parameters.

Parameters (Unit)	Value
K_1 (s mol kg^{-1} m^{-2})	9.32×10^{-4}

K_2 (Pa^{-1})	1.25×10^{-3}
K_3 (Pa^{-1})	3.82×10^{-5}
K_4 (s mol kg^{-1} m^{-2})	2.19×10^{-3}
K_5 (Pa^{-1})	9.88×10^{-4}
K_6 (Pa^{-1})	8.13×10^{-5}

The nickel-catalyzed water gas shift reaction (WGSR) ($CO+H_2O\leftrightarrow CO_2+H_2$) in the anode electrode is also an important chemical reaction and is fully considered in the model. This reaction converts CO into H_2 and ensures H_2 to mainly participate in electrochemical reaction. The reaction rate of WGSR [40] is expressed in Eqn. (3).

$$\begin{cases} r_{WGSR} = a(P_{H_2O}P_{co} - \dfrac{P_{H_2}P_{co_2}}{b}) \\ a = 0.0171e^{\frac{-103191}{RT}}\ (\mathrm{mol}\,m^{-3}\,Pa^{-2}\,s^{-1}) \\ b = e^{(-0.2935Z^3+0.6351Z^2+4.1788Z+0.3169)} \qquad Z = \dfrac{1000}{T} - 1 \end{cases} \tag{3}$$

In summary, the water gasification reaction replaces the Boudouard reaction and becomes the main chemical reaction for H_2O case. It should be noted that the electrochemical oxidation of H_2 is much easier than that of CO in SOFC. By introducing H_2O into DC-SOFCs, better electrochemical reaction activity can be achieved due to more rapid gas fuel production rate.

2.2.2. Electrochemical reactions

For the CO_2 case, the CO is the only fuel that is electrochemically oxidized in the DC-SOFC anode. While for the H_2O case, both CO and H_2 will be produced in the chemical reactions and participate in the electrochemical reactions: $CO+O^{2-}\rightarrow CO_2+2e^-$, and $H_2+O^{2-}\rightarrow H_2O+2e^-$.

The operating potential V is expressed in terms of the thermodynamic equilibrium potential E_{eq} and operating activation/ohmic overpotential losses in Eqn. (4).

$$V = E_{eq} - \eta_{ohmic} - \eta_{act} \tag{4}$$

where η_{ohmic} and η_{act} are the ohmic overpotential and activation overpotentials, respectively. The η_{ohmic} is related to the ionic/electronic conductivity and current intensity of the cell. More detailed information can be found in our previous work [41-43]. The potential obstacle for the electrochemical reaction is expressed as the activation overpotential η_{act}. The relationship between the η_{act} and the current density can be described by the Butler-Volmer equation as shown in Eqn. (5).

$$i = i_0(e^{\frac{nF\alpha\eta_{act}}{RT}} - e^{\frac{nF(1-\alpha)\eta_{act}}{RT}}) \tag{5}$$

where the α and n is the charge transfer coefficient and the number of electrons transferred per electrochemical reaction, respectively. The exchange current density (i_0) related to the fuel

property and electrode material, is further expressed as Eqn. (6).

$$i_0 = \gamma e^{-\frac{E_{act}}{RT}} \tag{6}$$

where the γ and E_{act} are the pre-exponential factor and the activation energy level, respectively. In the present study, the typical values of γ and E_{act} are adopted and listed in Table 4.

The E_{eq} is determined by the thermodynamic properties of the reaction: reaction enthalpy, entropy, and Gibbs free energy. For the CO_2 case, the equilibrium potential can be calculated by the Nernst equation, since only CO participate in the electrochemical reaction, as shown in Eqn. (7). However, both CO and H_2 can take part in the electrochemical reaction for the H_2O case. The E_{eq} for CO/H_2 fuels can be determined by Eqns. (7-8) respectively in this situation. Noted that the E_{eq} calculated by Eqns. (7-8) are equal under an open-circuit condition. The E_{eq} for CO and H_2 fuels become different, when current is extracted from the DC-SOFC, due to the different overpotential losses involved in electrochemical oxidation of the CO/H_2 fuel.

$$E_{CO} = E^0_{CO} + \frac{RT}{2F}\ln\left[\frac{P^l_{CO}(P^l_{O_2})^{0.5}}{P^l_{CO_2}}\right] \tag{7}$$

$$E_{H_2} = E^0_{H_2} + \frac{RT}{2F}\ln\left[\frac{P^l_{H_2}(P^l_{O_2})^{0.5}}{P^l_{H_2O}}\right] \tag{8}$$

where the E^0 and P^l are the standard potential and the local gas partial pressure, respectively. Then the values of the standard potential of carbon monoxide oxidization and hydrogen are expressed in Eqn. (9).

$$\begin{cases} E^0_{CO} = 1.46713 - 0.00045270T \\ E^0_{H_2} = 1.25300 - 0.00024516T \end{cases} \tag{9}$$

Table 4. Electrochemical reaction parameters.

Parameters (Unit)	Value
γ_{H_2} (A m^{-2})	2.944×10^{10}
E_{act,H_2} (J mol^{-1})	1.2×10^{5}
γ_{O_2} (A m^{-2})	1.390×10^{9}
E_{act,O_2} (J mol^{-1})	1.2×10^{5}
γ_{CO} (A m^{-2})	1.673×10^{9}
$E_{act,CO}$ (J mol^{-1})	1.2×10^{5}

2.3. Heat and Mass Transfer Model

For the fluid flow, the classic Navier-Stokes equation with the Darcy's term is adopted to describe the momentum transport of gas species in both the gas channel and the porous electrodes as shown in Eqn. (10)

$$\rho \frac{\partial u}{\partial t} + \rho u \nabla u = -\nabla p + \nabla \left[\mu (\nabla u + (\nabla u)^T) - \frac{2}{3} \mu \nabla u \right] - \frac{\varepsilon \mu u}{k} \tag{10}$$

When the last term on the right side of the Eqn. (10) is removed, the equation is simplified to the traditional N-S equation for momentum conservation of gas flows. k is the permeability of the porous electrodes. ε is the porosity of the porous electrodes.

For the mass transport, the rate N_i in channels and the porous electrodes can be expressed by the general Fick's model [44] as:

$$N_i = \frac{1}{RT} (D_i^{eff} \frac{\partial (y_i P)}{\partial z} - \frac{B_0 y_i P}{\mu} \frac{\partial P}{\partial z}) \tag{11}$$

where the B_0 and y_i are the permeability coefficient of the porous electrodes and the mole fraction of component i (i=1, 2 ,…, n), respectively. The effective diffusion coefficient of component i is expressed as D_i^{eff} and can be further expressed as Eqn. (12) [45] for gas diffusion in the porous electrodes.

$$D_i^{eff} = \frac{\varepsilon}{\tau} (\frac{1}{D_{ik}^{eff}} + \frac{1}{D_{im}^{eff}})^{-1} \tag{12}$$

where τ is the tortuosity factor. The D_{ik}^{eff} and D_{im}^{eff} represent the effective Knudsen diffusion coefficient and the effective molecular diffusion coefficient. The detailed information on diffusion coefficient of D_{ik}^{eff} and D_{im}^{eff} can be found in Ref. [46].

Besides, for the heat transfer model, the electrochemical reactions in TPB sites generates heat while the carbon gasification in the anode chamber is highly endothermic. It not only results in the temperature gradient along the cell length, but also along the radial direction. Thus the general heat balance equation is applied to simulate the heat transfer process as Eqn. (13).

$$\rho C_p u \cdot \nabla T + \nabla \cdot (-\lambda_{\text{eff}} \nabla T) = Q \tag{13}$$

where the C_p and λ are the fluid thermal capacity and the thermal conductivity, respectively. In this equation, the λ_{eff} depends on the heat conductivity of liquid and solid phase, λ_s and λ_l, as the form of λ_{eff}= (1-ε) λ_s+$\varepsilon\lambda_l$ in the porous structure of electrodes. The Q is the heat source term, which represents the heat generation or consumption due to various overpotential losses and chemical/electrochemical reactions. In this paper, the heat source term contains heat consumption of carbon gasification and heat generation of CO electrochemical reaction, H_2 electrochemical reaction, ohmic overpotential and activation overpotential.

$$\Delta G = \Delta H - T \Delta S \tag{14}$$

ΔG is the Gibbs free energy for electricity generation which involves the ohmic overpotential

and activation overpotential. ΔH is the reaction enthalpy which is the heat consumption of carbon gasification. $T\Delta S$ is the irreversible loss of CO electrochemical reaction and H_2 electrochemical reaction.

2.4. Model solution and verification

A given gas temperature is specified at the channel inlet. The outer boundary of the cathode chamber, the end of electrodes and electrolyte are thermally insulated. Inflow gas mole fraction and flow rate are given at the channel inlets. The outflow condition is specified at the outlets of the gas channels. Zero flux is specified at the end of the electrodes and pressure condition is specified at the outlets of the two gas channels. Electric potentials are specified at the two electrodes. Two ends of the cell are electrically insulated.

The model is solved at given operating conditions such as operating potential, inlet gas temperature, anode inlet gas flow rate, and the distance between carbon and anode. The output of the model includes temperature distribution, mole fraction of gas species, chemical reaction rates, and distributions of the electrochemical reaction rates in the cell. The commercial software COMSOL MULTIPHYSICS is employed for the numerical simulation.

This model is an extension of our previous model, which has already been validated with experimental data from the literature (Fig. 2(b,c)). More detailed information about the model validation can be found in [18]. In order to ensure grid-independence, six meshes of H_2O case are used for the preliminary simulations, respectively, with 30 thousand, 79 thousand, 153 thousand, 196 thousand, 237 thousand and 297 thousand cells by regulating the number of nodes. Current density and net heat generation are employed to evaluate the independence of the grids. The results are shown in Fig. 2(a). It is clear that there is a relatively large deviation between the results using the first three meshes. The numerical result of 236,777 cells has little difference with that of the 297,390 cells, showing a maximum deviation of 0.14%, which is acceptable. Therefore, the mesh of 236,777 cells is used for calculations.

3. Results and Discussion

3.1. Effect of Operating Voltage

The effects of operating on the current density, power density and the average cell temperature are shown in Fig. 3 (a-b). The detailed operating conditions are listed in Table 5.

Table 5. Operation parameters for operating potential effect study in DC-SOFCs.

Parameters (Unit)	Value
Operating potential (V)	0~0.8
Anode inlet gas flow rate (SCCM)	10

Cathode inlet gas flow rate (SCCM)	400
Anode gas composition for H_2O/CO_2 assisted DC-SOFC	100%
Cathode gas composition	Air
Temperature (K)	1123

It is found that the performance of DC-SOFCs with H_2O as agent is much higher than that with CO_2 as agent, which is consistent with the previous study [17, 18]. For DC-SOFCs with H_2O agent, the peak power density reaches 3713 W m^{-2} at 0.42 V, which is more than two times of that with CO_2 agent (1395 W m^{-2} at 0.56 V). The operating voltage decreases rapidly with a further increase in current density due to the huge concentration polarization. When operating potential decreases from 0.8 V to 0.1 V, the cell current density is found to increase from 831 A m^{-2} to 12308 A m^{-2} for the H_2O case and from 596 A m^{-2} to 2972 A m^{-2} for the CO_2 case. The average cell temperature increases when the operating potential increases from 1116 K at 0.8 V to 1195 K at 0.1 V in H_2O case and from 1122 K at 0.8 V to 1154 K at 0.1 V in CO_2 case as shown in Fig.3(b).

The significantly higher performance of H_2O-assisted DC-SOFC is due to the enhanced carbon gasification rate and the electrochemical oxidation of H_2 fuel in the anode. As can be seen in Fig.4. In Fig.4(a), the carbon gasification rate in H_2O assisted DC-SOFC ranges from 6.677 mol m^{-3} s^{-1} to 25.53 mol m^{-3} s^{-1} at 1123 K and 0.5 V operating potential. While the carbon gasification rate in CO_2 assisted DC-SOFC only ranges from 1.883 mol m^{-3} s^{-1} to 19.4 mol m^{-3} s^{-1}. The high-value zone has obviously greater proportion in H_2O case. More rapid carbon gasification kinetics by H_2O agent offers a higher mole fraction of the fuel for electrochemical reactions (both H_2 and CO). Consequently, the fuel mole fraction (CO + H_2) in H_2O case is much higher than that (CO) in CO_2 case as shown in Fig. 4(b). In H_2O case, H_2 takes part in the electrochemical reaction together with CO, so that a much higher electrochemical reaction rate is obtained, which could be found from Fig. 4(c). Fig. 4(c) is a partially enlarged view of anode near the electrolyte and position at the middle of the cell. The anode electrochemical reaction rate in H_2O assisted DC-SOFC ranges from -18.6 mol m^{-3} s^{-1} to 4.2×10^4 mol m^{-3} s^{-1} while that of CO_2 assisted DC-SOFCs ranges from -1 mol m^{-3} s^{-1} to 5.06×10^3 mol m^{-3} s^{-1}.

The temperature distribution of the DC-SOFC is shown in Fig.5. The different temperature distribution patterns are caused by the different chemical and electrochemical processes in the DC-SOFC. In Fig.5(a,c), it is found that the temperature increases along the cell length, the peak temperature occurs at anode/electrolyte interface and the anode chamber temperature is always lower than the cathode channel temperature, which are consistent with the result in Fig.4, as the endothermic carbon gasification reaction takes place in the anode chamber and the electrochemical reaction takes place in the narrow region near the anode/electrolyte interface. Compared to 0.1V, the heat generation from electrochemical reaction and overpotential losses

is lower that of at 0.5V, leading to a lower cell temperature. Compared to CO_2 case, exothermic processes are greatly enhanced in H_2O case due to the higher current density, which in turn increases the temperature, which could also be explained in Fig.5 (b,d) by the more significant oxygen consumption.

In order to gain a fundamental understanding of the thermal effect, Fig.6 (a,c) show a breakdown on heat consumption/generation from different components in the cell and Fig.6 (b,d) show the percentages of different heat sources. The CER represents CO electrochemical reaction, HER represents H_2 electrochemical reaction, OO represents ohmic overpotential, AO represents activation overpotential, CG represents carbon gasification and NH represents net heat of the whole cell.

More heat generation is caused by the increasing overpotential losses and electrochemical reaction rate with decreasing operating potential. On the other hand, more CO_2/H_2O can be generated at a higher current density, which increases the rate of the endothermic carbon gasification reaction and more heat consumption. These combined effects result in the slightly different temperature increase and net heat generation when voltage decreases, which well explains the Fig.3 (b). The electrochemical reaction (CER in CO_2 case and CER+HER in H_2O case) contributes most to the heat generation at high potential and the contribution of ohmic overpotential and activation overpotential increases with the decreasing potential. In addition, due to the both higher heat generation and consumption compared with CO_2 case, the cell temperature distribution in the H_2O case is less uniform at a low operating potential, which increases the thermal stress in the cell and suffers from poor durability under changing operating potential.

As shown in Fig.6, the net heat is changed from negative to positive when the operating voltage is decreased. The results suggest that there is thermal-neutral voltage, at which the cell is thermally self-sustained and no heat supply/removal is needed.

3.2. Effect of Anode Inlet Gas Flow Rate

The operating conditions of DC-SOFCs with both two agents are listed in Table 6. As shown in Fig.7 (a), for both H_2O assisted DC-SOFC and CO_2 assisted DC-SOFC, the increase of anode inlet gas flow rate has a negative effect on the cell performance. With the anode inlet gas flow rate increasing from 1 SCCM to 50 SCCM, the current density of the CO_2 case decreases from 2741 A m^{-2} to 2434 A m^{-2}. This is mainly due to the CO_2 produced by electrochemical reaction is already enough for carbon gasification and the increased flowrate of CO_2 will only dilute the fuel in DC-SOFC. For the H_2O case, the current density decreases from 7069 A m^{-2} to 6488 A m^{-2} while the anode inlet gas flow rate increasing from 1 SCCM to 50 SCCM. Although the

carbon gasification rate is faster with higher flowrate of H_2O or CO_2 to produce more fuel, the temperature of both the H_2O case and CO_2 case decreases with the increasing inlet flow rate, which is shown in Fig. 7(b), as faster flow of gasification agents causes faster heat consumption of carbon gasification and takes away more heat. As the inlet gas flow rate continues to increase, the steam carbon gasification rate cannot be further increased with the increasing inlet gas flow rate. Furthermore, fuels (H_2 and CO) in anode can be also diluted by the increasing gas flow rate of H_2O or CO_2 and have less molar fractions as shown in Fig. 8(a), which results in the decrease of the current density of DC- SOFC.

Table 6. Operation parameters for anode inlet gas flow rate effect study in DC-SOFCs.

Parameters (Unit)	Value
Operating potential (V)	0.5
Anode inlet gas flow rate (SCCM)	1~50
Cathode inlet gas flow rate (SCCM)	400
Anode gas composition for H_2O/CO_2 assisted DC-SOFC	100%
Cathode gas composition	Air
Temperature (K)	1123

Although the endothermic carbon gasification rate is much higher in H_2O case, it can be seen in Fig.8 that the temperature of the anode chamber is higher than that in the CO_2 case, as the higher anode temperature enhances the heat transfer between the porous anode and the anode chamber. Compared with CO_2 case, it is obvious that the temperature of carbon layer near the anode increases along the cell length in the H_2O case, as more high temperature gas (H_2O/CO_2) produced by electrochemical reactions at the anode also accelerates the heat transfer.

It can be seen from Fig.9 that the anode inlet gas flow rate only has very slight effect on heat composition both in the H_2O case and the CO_2 case. Above all, the results suggest that a high anode inlet gas flow rate is not necessary for DC-SOFC.

From the present study, it is clear that the thermal effect is significant as there could be large temperature gradient in the cell, which not only affect the performance but also the durability of the DC-SOFC.

3.3. Effect of Inlet Gas Temperature

The operating conditions of DC-SOFCs at different temperatures are listed in Table 7. As can be seen from Fig. 10(a), the current density of both the H_2O case and the CO_2 case is increased at a higher temperature. Both electrochemical reaction kinetics and chemical reaction kinetics benefits from the increase of operating temperature. For the CO_2 case, with temperature

increasing from 1073 K to 1173 K, the current density is greatly increased from 1151 A m^{-2} to 5352 A m^{-2}. This substantial increase indicates that a relative higher temperature is needed for the CO_2 case as Boudouard reaction rate is quite slow at a lower temperature. For the H_2O case, the current density is 3625 A m^{-2} at 1073 K, which is more than 3 times of the current density of the CO_2 case at the same temperature. This result suggests that, even at relatively lower temperature, the H_2O case still has an acceptable output power density. When the operating temperature reaches 1103 K, the current density of the H_2O case reaches 5470 A m^{-2}, exceeding the current density of the CO_2 case at 1173 K. Finally, the H_2O case achieves 11369 A m^{-2} at 1173 K, which is more than 2 times higher than that of CO_2 assisted DC- SOFCs. Thus, using H_2O as agent is very promising for DC-SOFC at a wider range of temperature.

Table 7. Operation parameters for temperature effect study in DC-SOFCs.

Parameters (Unit)	Value
Operating potential (V)	0.5
Anode inlet gas flow rate (SCCM)	10
Cathode inlet gas flow rate (SCCM)	400
Anode gas composition for H_2O/CO_2 assisted DC-SOFC	100%
Cathode gas composition	Air
Temperature (K)	1073~1173

In the Fig.10 (b), it can be seen that there is only slight difference in average cell temperature between the H_2O case and the CO_2 case. Combining Fig.8 and Fig.10, it can be found that the temperature distribution difference between H_2O and CO_2 case is smaller at 1173K than at 1073K. This result can be explained in Fig.12. The net heat is almost zero in most cases due to the almost same heat generation and consumption. With increasing temperature, the carbon gasification, the electrochemical reaction and the overpotential losses are all increased, which leads to thermal neutral status. The net heat in CO_2 case all remains around zero, while the net heat in the H_2O case slight increases then slight decreases with increasing temperature. This is because more H_2O and CO_2 can be generated at a higher current density at higher inlet temperature, which increases the rate of the endothermic carbon gasification and the heat consumption in the anode chamber.

3.4. Effect of Distance Between Carbon and Anode

Previous study has shown how the distance between carbon fuel and anode, D_{ce}, have affect the performance of DC-SOFC [34]. The increase of D_{ce} will increase the variation of temperature in the cell due to different thermal conductivity between solid carbon and gas. Thus the effect of D_{ce} on the temperature distribution of the cell is discussed. Detailed operating

parameters are listed in Table 8.

Table 8. Operation parameters for D_{ce} effect study in DC-SOFCs.

Parameters (Unit)	Value
Operating potential (V)	0.5
Distance between anode chamber and electrode, D_{ce} (μm)	50~2050
Anode inlet gas flow rate (SCCM)	10
Cathode inlet gas flow rate (SCCM)	400
Anode gas composition for H_2O/CO_2 assisted DC-SOFC	100%
Cathode gas composition	Air
Temperature (K)	1123

Fig. 13 shows the effects of D_{ce} on the temperature distribution in the cell with 1123 K inlet gas temperature and 0.5 V operating potential. Distance between carbon and anode surface is varied from 50 μm to 2050 μm in this study. As can be seen from Fig.13, when D_{ce} is quite small (50 μm), the gradient along the cell width is small. The uniform temperature distribution is desirable to reduce the thermal stress in the cell for long-term and stable operation of DC-SOFC. With the increase of D_{ce}, there occurs an obvious temperature boundary between solid carbon and anode gas channel and the gradient along the cell width becomes quite large both in H_2O and CO_2 cases. Combining Fig.14 and Fig.15, it can be observed that, with the increase of D_{ce}, the fuel gas molar fraction in anode decreases quickly while the O_2 molar fraction in cathode channel is increasing, which means the electrochemical reaction rate and overpotential losses are decreasing, due to the increased gas transport difficulty and lower chemical reaction temperature caused by larger D_{ce}. Therefore, the performance of the DC-SOFC can be decreases with the increasing D_{ce}.

As stated, larger D_{ce} causes lower anode chamber temperature. However, it is found that the temperature of cell first increases and then decreases, which is due to the combination of two factors. On the one hand, larger D_{ce} weakens the heat transfer between the porous anode and the anode chamber, which tends to increase the anode temperature due to the electrochemical processes. On the other hand, the heat generation is declining with increasing D_{ce}, as can be clearly seen in Fig.16. Thus, with a further increase in D_{ce}, the generated heat due to electrochemical process in the anode can no longer maintain a high temperature in the cell. Besides, it is observed from Fig.16 that the electrochemical reaction and overpotential losses in the H_2O case are always much higher than the CO_2 case at same D_{ce}, due to higher current density in the H_2O case. The percentages of overpotential losses heat account higher in H_2O case compared with CO_2 case. Above all, it is important to keep a small distance between the carbon fuel and anode to achieve good cell performance when cell is placed horizontally.

4. Conclusion

A multi-physics model is developed to investigate the thermal effect in H_2O and CO_2 assisted tubular DC-SOFCs. The model fully considers the heat transfer, mass transport, momentum transport, chemical reactions, electrochemical reactions and transport of ions/electrons processes in the DC-SOFC. Parametric simulations are further conducted to study the effects of operating potential, the distance between carbon and anode, inlet gas temperature, and anode inlet gas flow rate on the thermal behaviors of DC-SOFC. It is found that the temperature field in DC-SOFC is highly non-uniform, which not only affect the performance but also the durability of the DC-SOFC.

Benefiting from higher cell temperature, faster carbon gasification rate, higher fuel concentration in anode and faster electrochemical reaction kinetics, DC-SOFC with H_2O as gasification agent performs considerably better than the DC-SOFC with CO_2 as gasification agent in all cases. The breakdown of heat sources of DC-SOFC shows that the H_2O assisted DC-SOFC has much higher heat generation and consumption than CO_2 assisted DC-SOFC. A thermal neutral voltage is observed, at which the cell is thermally self-sustained and no heat supply/removal is needed. High anode inlet gas flow rate is not necessary due to its slight effect on heat composition both in the H_2O case and the CO_2 case. With increasing inlet gas temperature, the net heat is almost zero in most cases due to the almost same heat generation and consumption. In addition, the distance between the anode and the carbon layer is required to be as small as possible, which benefits the improvement of the temperature uniformity and performance of the DC-SOFC.

The paper provided useful information on the thermal effects of various parts of the fuel cell along the radial direction and the general temperature trend along the length direction. Although the information of temperature and species distribution along the flow direction is provided as well, more detailed simulation and analyses are needed since the simulated cell is very short with a length of only 10mm. Simulations of larger cells with more practical dimensions are needed for cell design and optimization. Above all, the results of this study conclusively shows that the importance of thermal effects in DC-SOFCs and form a solid foundation for DC-SOFC thermal management.

Acknowledgement

This research is supported by a grant under the Theme-based Scheme (project number: T23-601/17-R) from Research Grant Council, University Grants Committee, Hong Kong SAR.

References

[1] Ni M. 2D thermal modeling of a solid oxide electrolyzer cell (SOEC) for syngas production by H_2O/CO_2 co-electrolysis. International Journal of Hydrogen Energy 2012; 37(8): 6389-6399.

[2] Ni M, Leung M K H, Leung D Y C. Energy and exergy analysis of hydrogen production by a proton exchange membrane (PEM) electrolyzer plant. Energy Conversion and Management 2008; 49(10): 2748-2756.

[3] Tan P, Liu M, Shao Z, et al. Recent advances in perovskite oxides as electrode materials for nonaqueous lithium–oxygen batteries. Advanced Energy Materials 2017; 7(13): 1602674.

[4] Yu J, Wu X, Zhong Y, et al. Multifold Nanostructuring and Atomic‐Scale Modulation of Cobalt Phosphide to Significantly Boost Hydrogen Production. Chemistry–A European Journal 2018; 24(52): 13800-13806.

[5] Wu Z, Tan P, Zhu P, et al. Performance analysis of a novel SOFC-HCCI engine hybrid system coupled with metal hydride reactor for H_2 addition by waste heat recovery. Energy Conversion and Management 2019; 191: 119-131.

[6] Zhang HC, Kong W, Dong FF, Xu HR, Chen B, Ni M. Application of cascadeing thermoelectric generator and cooler for waste heat recovery from solid oxide fuel cells, Energy Conversion and Management 2017; 148: 1382-1390.

[7] Xu H, Chen B, Tan P, et al. Modeling of all porous solid oxide fuel cells. Applied Energy 2018; 219: 105-113.

[8] Cai W, Liu P, Chen B, et al. Plastic waste fuelled solid oxide fuel cell system for power and carbon nanotube cogeneration. International Journal of Hydrogen Energy 2019; 44(3): 1867-1876.

[9] Chen B, Xu H, Tan P, et al. Thermal modelling of ethanol-fuelled Solid Oxide Fuel Cells. Applied Energy 2019; 237: 476-486.

[10] Wu Z, Tan P, Chen B, et al. Dynamic modeling and operation strategy of an NG-fueled SOFC-WGS-TSA-PEMFC hybrid energy conversion system for fuel cell vehicle by using MATLAB/SIMULINK. Energy 2019; 175: 567-579.

[11] Nakagawa N, Ishida M. Performance of an internal direct-oxidation carbon fuel cell and its evaluation by graphic exergy analysis. Industrial & Engineering Chemistry Research 1988; 27(7): 1181-1185.

[12] Liu R, Zhao C, Li J, et al. A novel direct carbon fuel cell by approach of tubular solid oxide fuel cells. Journal of Power Sources 2010; 195(2): 480-482.

[13] Bai Y, Liu Y, Tang Y, et al. Direct carbon solid oxide fuel cell—a potential high performance battery. International Journal of Hydrogen Energy 2011; 36(15): 9189-9194.

[14] Wu Y, Su C, Zhang C, et al. A new carbon fuel cell with high power output by integrating with in situ catalytic reverse Boudouard reaction. Electrochemistry Communications 2009; 11(6): 1265-1268.

[15] Jiao Y, Zhao J, An W, et al. Structurally modified coal char as a fuel for solid oxide-based carbon fuel cells with improved performance. Journal of Power Sources 2015; 288: 106-114.

[16] Dudek M, Tomov R I, Wang C, et al. Feasibility of direct carbon solid oxide fuels cell (DC-SOFC) fabrication by inkjet printing technology. Electrochimica Acta 2013, 105: 412-418.

[17] Wang W, Liu Z, Zhang Y, et al. A direct carbon solid oxide fuel cell stack on a single electrolyte plate fabricated by tape casting technique. Journal of Alloys and Compounds 2019, 794: 294-302.

[18] Guo Y , Bessaa M , Aguado S , et al. An all porous solid oxide fuel cell (SOFC): a bridging technology between dual and single chamber SOFCs. Energy & Environmental Science 2013, 6(7):2119.

[19] Wu W, Ding D, Fan M, et al. A High Performance Low Temperature Direct Carbon Fuel Cell. ECS

Transactions 2017, 78(1): 2519.
[20] Wu H, Xiao J, Zeng X, et al. A high performance direct carbon solid oxide fuel cell–A green pathway for brown coal utilization. Applied Energy 2019, 248: 679-687.
[21] Zhou M, Wang X, Zhang Y, et al. Effect of counter diffusion of CO and CO_2 between carbon and anode on the performance of direct carbon solid oxide fuel cells. Solid State Ionics 2019, 343: 115127.
[22] Wang C, Lü Z, Su C, et al. Effects of discharge mode and fuel treating temperature on the fuel utilization of direct carbon solid oxide fuel cell. International Journal of Hydrogen Energy 2019, 44(2): 1174-1181.
[23] Lee A C, Mitchell R E, Gür T M. Thermodynamic analysis of gasification-driven direct carbon fuel cells. Journal of Power Sources 2009; 194(2): 774-785.
[24] Ong K M, Ghoniem A F. Modeling of indirect carbon fuel cell systems with steam and dry gasification. Journal of Power Sources 2016; 313: 51-64.
[25] Xu H, Chen B, Zhang H, et al. Modeling of direct carbon solid oxide fuel cells with H_2O and CO_2 as gasification agents. International Journal of Hydrogen Energy 2017; 42(23): 15641-15651.
[26] Xu H, Chen B, Zhang H, et al. Experimental and modeling study of high performance direct carbon solid oxide fuel cell with in situ catalytic steam-carbon gasification reaction. Journal of Power Sources 2018; 382: 135-143.
[27] Tai L W, Nasrallah M M, Anderson H U, et al. Structure and electrical properties of $La_{1-x}Sr_xCo_{1-y}Fe_yO_3$. Part 2. The system $La_{1-x}Sr_xCo_{0.2}Fe_{0.8}O_3$. Solid State Ionics 1995; 76(3-4): 273-283.
[28] Luo Y, Shi Y, Li W, et al. Comprehensive modeling of tubular solid oxide electrolysis cell for co-electrolysis of steam and carbon dioxide. Energy 2014; 70: 420-434.
[29] Shi Y, Cai N, Li C, et al. Modeling of an anode-supported Ni–YSZ| Ni–ScSZ| ScSZ| LSM–ScSZ multiple layers SOFC cell: Part I. experiments, model development and validation. Journal of Power Sources 2007; 172(1): 235-245.
[30] Eguchi K. Ceramic materials containing rare earth oxides for solid oxide fuel cell. Journal of Alloys and Compounds 1997; 250(1-2): 486-491.
[31] Fan B, Yan J, Yan X. The ionic conductivity, thermal expansion behavior, and chemical compatibility of $La_{0.54}Sr_{0.44}Co_{0.2}Fe_{0.8}O_{3-\delta}$ as SOFC cathode material. Solid State Sciences 2011; 13(10): 1835-1839.
[32] Lee S, Kim H, Yoon K J, et al. The effect of fuel utilization on heat and mass transfer within solid oxide fuel cells examined by three-dimensional numerical simulations. International Journal of Heat and Mass Transfer 2016; 97: 77-93.
[33] Waller D, Lane J A, Kilner J A, et al. The effect of thermal treatment on the resistance of LSCF electrodes on gadolinia doped ceria electrolytes. Solid State Ionics 1996; 86: 767-772.
[34] Shin Y C, Hashimoto S, Yashiro K, et al. Thermal Properties of Perovskite-Type Oxides $La_{0.6}Sr_{0.4}Co_{1-x}Fe_xO_{3-\delta}$ ($0 \leq x \leq 1.0$). ECS Transactions 2016; 72(7): 105-110.
[35] Zhang H, Lv J, Li G, et al. Investigation about thermophysical properties of $Ln_2Ce_2O_7$ (Ln= Sm, Er and Yb) oxides for thermal barrier coatings. Materials Research Bulletin 2012; 47(12): 4181-4186.
[36] Zhang X, Hamel P, Yick S, et al. A study of coarsening samarium doped ceria on interaction with yttria stabilized zirconia. ECS Transactions 2011; 35(1): 1211-1217.
[37] Hayashi H, Saitou T, Maruyama N, et al. Thermal expansion coefficient of yttria stabilized zirconia for various yttria contents. Solid state ionics 2005; 176(5-6): 613-619.
[38] Schlichting K W, Padture N P, Klemens P G. Thermal conductivity of dense and porous yttria-stabilized zirconia. Journal of Materials Science 2001; 36(12): 3003-3010.
[39] Huang Z, Zhang J, Zhao Y, et al. Kinetic studies of char gasification by steam and CO_2 in the presence of H2 and CO. Fuel Processing Technology, 2010, 91(8): 843-847.
[40] Ni M. Modeling of SOFC running on partially pre-reformed gas mixture. International Journal of

Hydrogen Energy 2012; 37(2): 1731-1745.
[41] Xu H, Chen B, Liu J, et al. Modeling of direct carbon solid oxide fuel cell for CO and electricity cogeneration. Applied Energy 2016; 178: 353-362.
[42] Xu H, Chen B, Ni M. Modeling of direct carbon-assisted solid oxide electrolysis cell (SOEC) for syngas production at two different electrodes. Journal of the Electrochemical Society 2016; 163(11): F3029-F3035.
[43] Xu H, Chen B, Irvine J, et al. Modeling of CH4-assisted SOEC for H_2O/CO_2 co-electrolysis. International Journal of Hydrogen Energy 2016; 41(47): 21839-21849.
[44] Suwanwarangkul R, Croiset E, Fowler M W, et al. Performance comparison of Fick's, dusty-gas and Stefan–Maxwell models to predict the concentration overpotential of a SOFC anode. Journal of Power Sources 2003; 122(1): 9-18.
[45] Chan S H, Khor K A, Xia Z T. A complete polarization model of a solid oxide fuel cell and its sensitivity to the change of cell component thickness. Journal of Power Sources 2001; 93(1-2): 130-140.
[46] Todd B, Young J B. Thermodynamic and transport properties of gases for use in solid oxide fuel cell modelling. Journal of power Sources 2002; 110(1): 186-200.

Figure Captions

Fig.1 Schematic of CO_2 assisted DC-SOFC (a) and H_2O assisted DC-SOFC (b).

Fig.2 Mesh independence (a) and model validation (b,c).

Fig.3 The voltage-current density-power density (a) and voltage-average cell temperature (b) relationships for CO_2 case and H_2O case.

Fig.4 The carbon gasification rate in carbon layer (a), the mole fraction of fuel in anode (b) and the anode electrochemical reaction rate (c) with CO_2 assisted (left) and H_2O assisted (right) DC-SOFCs at 0.5 V and 1123 K.

Fig.5 Cell temperature distribution with CO_2 (a) and H_2O (c) as agents and cathode O_2 molar fraction with CO_2 (b) and H_2O (d) as agents at 0.5 V (left) and 0.1 V (right).

Fig.6 Effects of applied voltage on the heat compositions including CO electrochemical reaction (CER), H_2 electrochemical reaction (HER), ohmic overpotential (OO), activation overpotential (AO) and carbon gasification (CG) and net heat (NH) with CO_2 (a) and H_2O (c) as agents and percentages of different heat sources with CO_2 (b) and H_2O (d) as agents.

Fig.7 The anode inlet gas flow rate-current (a) and anode inlet gas flow rate-average cell temperature (b) relationships of DC-SOFCs with CO_2 and H_2O as agents.

Fig.8 Effects of anode inlet gas flow rate on the fuel gas molar fraction distribution in the anode with CO_2 assisted (left) and H_2O assisted (right) DC-SOFCs at 0.5 V and 1123 K; Cell temperature distribution with CO_2 (b) and H_2O (c) as agents at 10 SCCM anode inlet gas flow rate.

Fig.9 Effects of anode inlet gas flow rate on the heat compositions including CO electrochemical reaction (CER), H_2 electrochemical reaction (HER), ohmic overpotential (OO), activation overpotential (AO) and carbon gasification (CG) and net heat (NH) with CO_2 (a) and H_2O (c) as agents and percentages of different heat sources with CO_2 (b) and H_2O (d) as agents.

Fig.10 The inlet gas temperature-current (a) and inlet gas temperature-average cell temperature (b) relationships of DC-SOFCs with CO_2 and H_2O as agents.

Fig.11 Cell temperature distribution with CO_2 (a) and H_2O (b) as agents at 0.5 V and 1173 K.

Fig.12 Effects of anode inlet gas flow temperature on the heat compositions including CO electrochemical reaction (CER), H_2 electrochemical reaction (HER), ohmic overpotential (OO), activation overpotential (AO) and carbon gasification (CG) and net heat (NH) with CO_2 (a) and H_2O (c) as agents and percentages of different heat sources with CO_2 (b) and H_2O (d) as agents.

Fig.13 Effects of D_{ce} on the temperature distribution in the cell with CO_2 assisted (left) and H_2O assisted (right) DC-SOFCs at 0.5 V and 1123 K.

Fig.14 Effects of D_{ce} on the fuel gas molar fraction distribution in the anode with CO_2 assisted (left) and H_2O assisted (right) DC-SOFCs at 0.5 V and 1123 K.

Fig.15 Effects of D_{ce} on the O_2 molar fraction distribution in the cathode with CO_2 assisted (left) and H_2O assisted (right) DC-SOFCs at 0.5 V and 1123 K.

Fig.16 Effects of D_{ce} on the heat compositions including CO electrochemical reaction (CER), H_2 electrochemical reaction (HER), ohmic overpotential (OO), activation overpotential (AO) and carbon gasification (CG) and net heat (NH) with CO_2 (a) and H_2O (c) as agents and percentages of different heat sources with CO_2 (b) and H_2O (d) as agents.

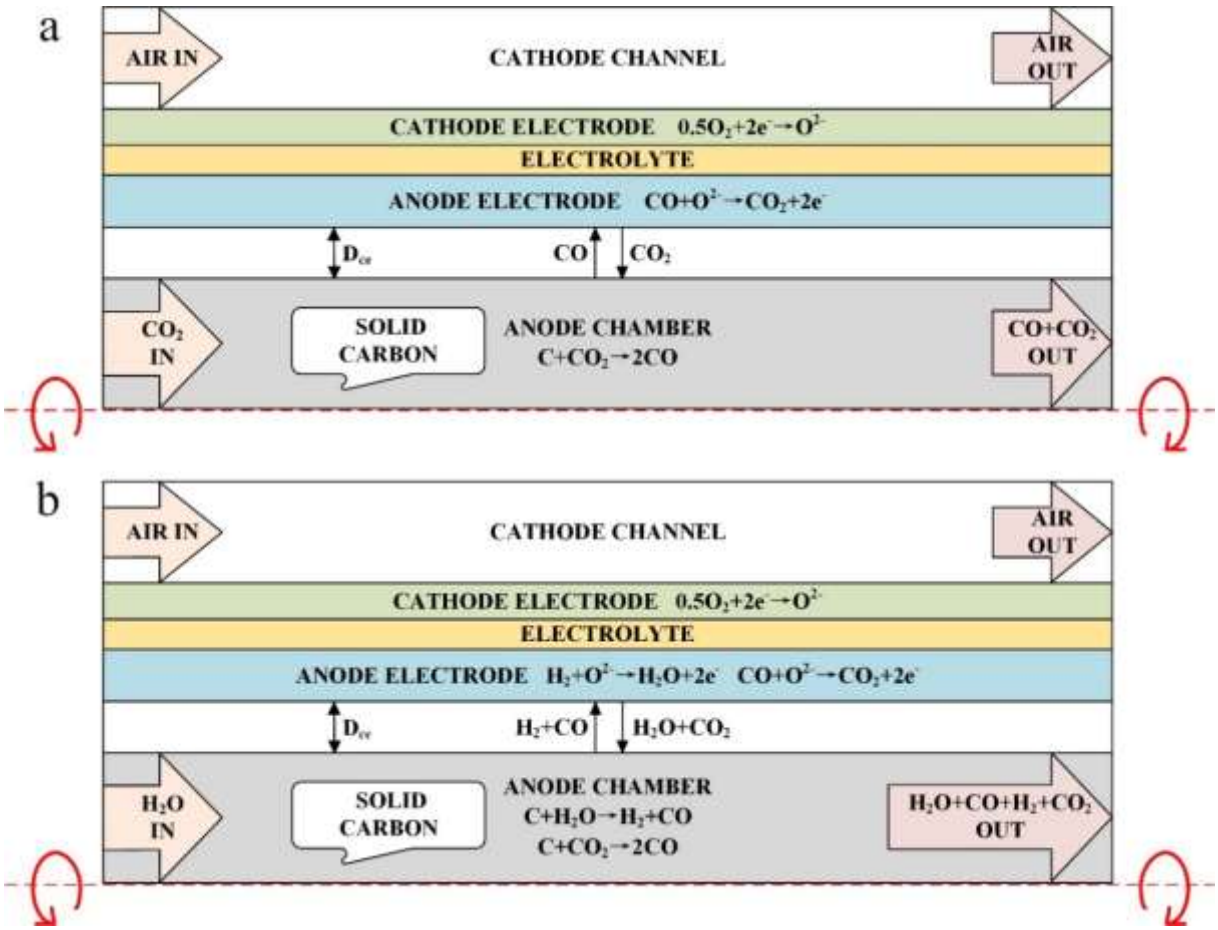

Fig.1 Schematic of CO_2 assisted DC-SOFC (a) and H_2O assisted DC-SOFC (b).

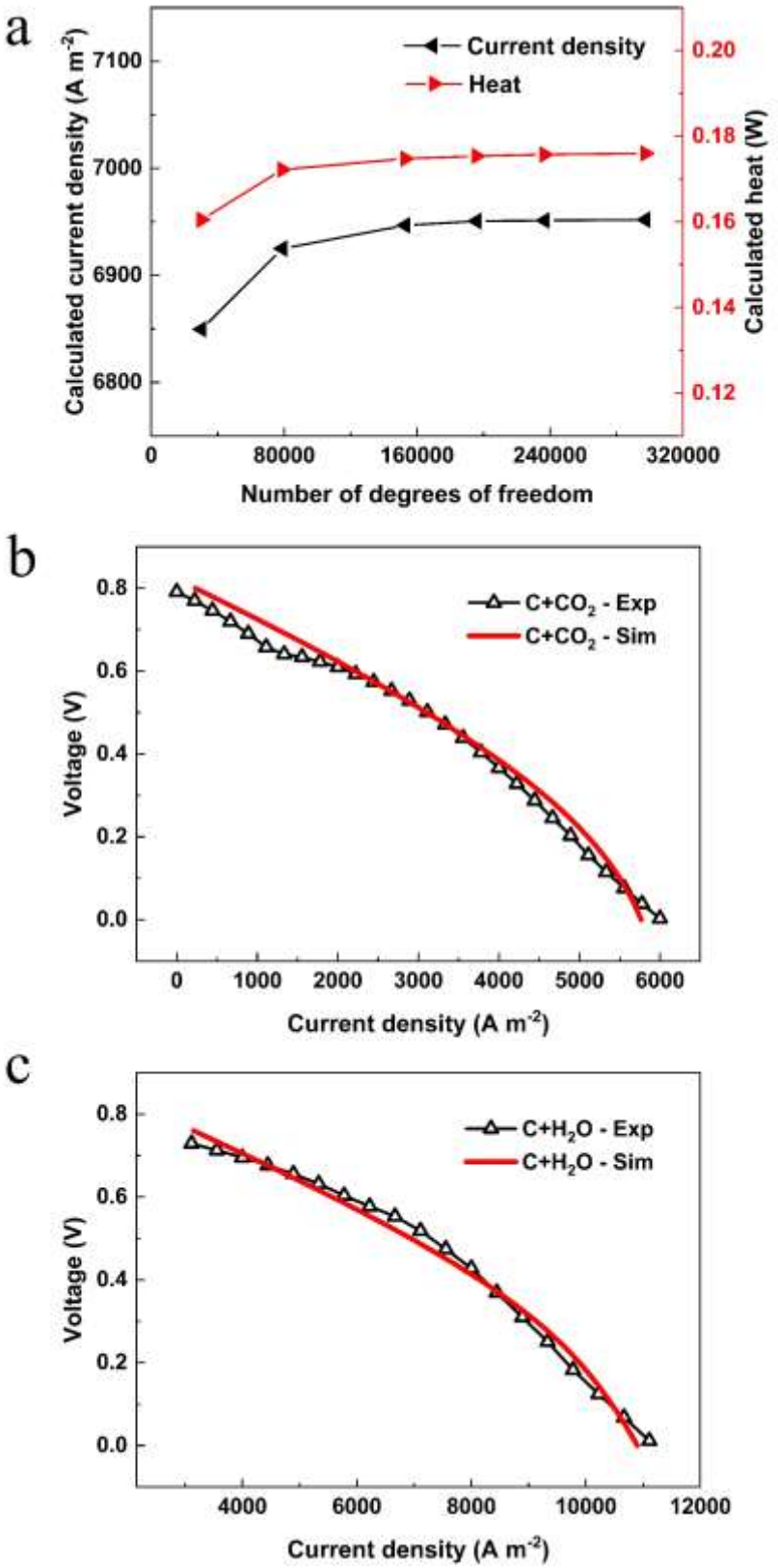

Fig.2 Mesh independence (a) and model validation (b,c).

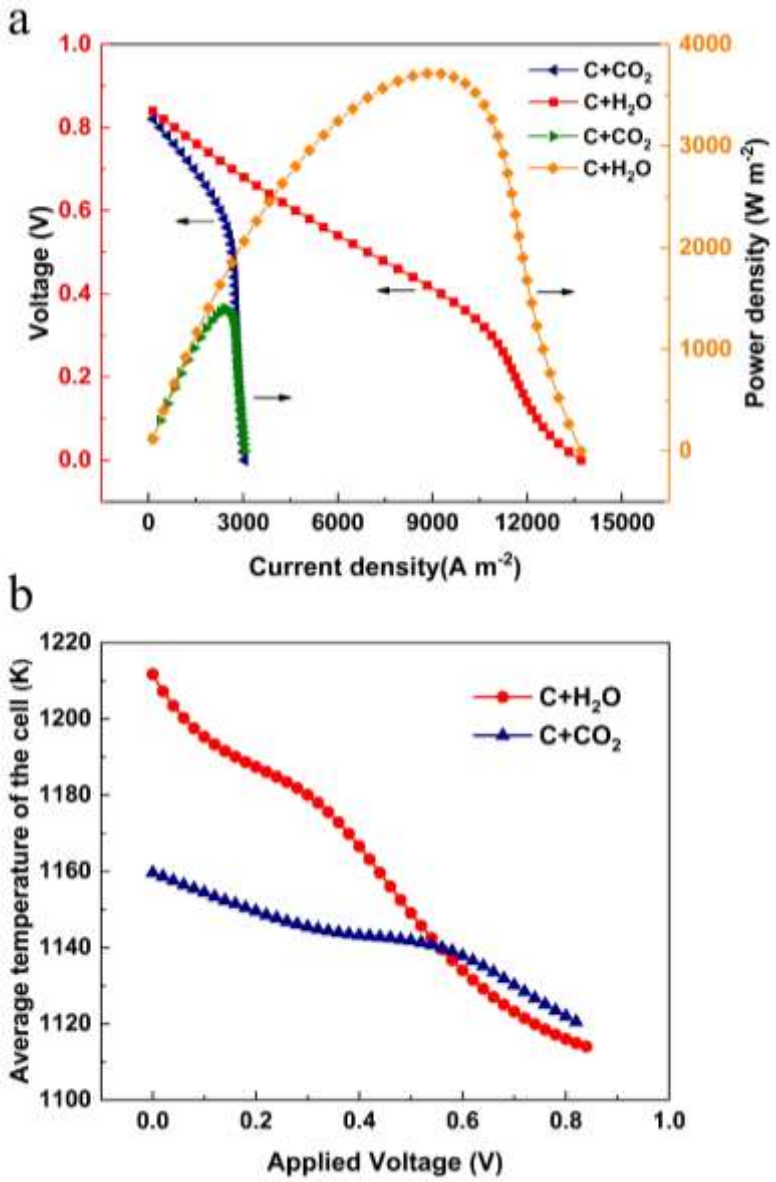

Fig.3 The voltage-current density-power density (a) and voltage-average cell temperature (b) relationships for CO_2 case and H_2O case.

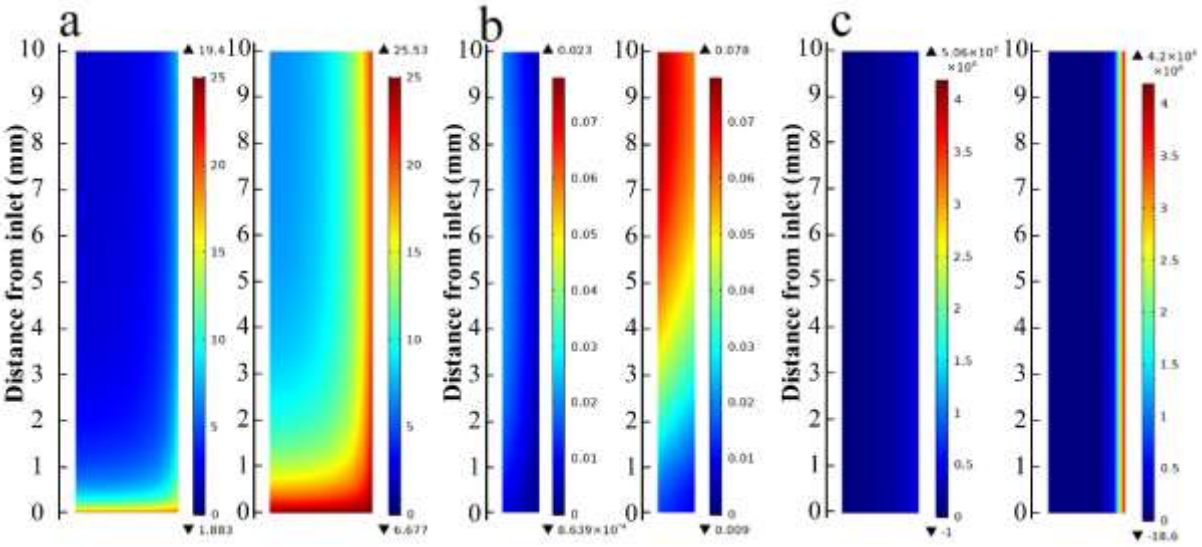

Fig.4 The carbon gasification rate in carbon layer (a), the mole fraction of fuel in anode (b) and the anode electrochemical reaction rate (c) with CO_2 assisted (left) and H_2O assisted (right) DC-SOFCs at 0.5 V and 1123 K.

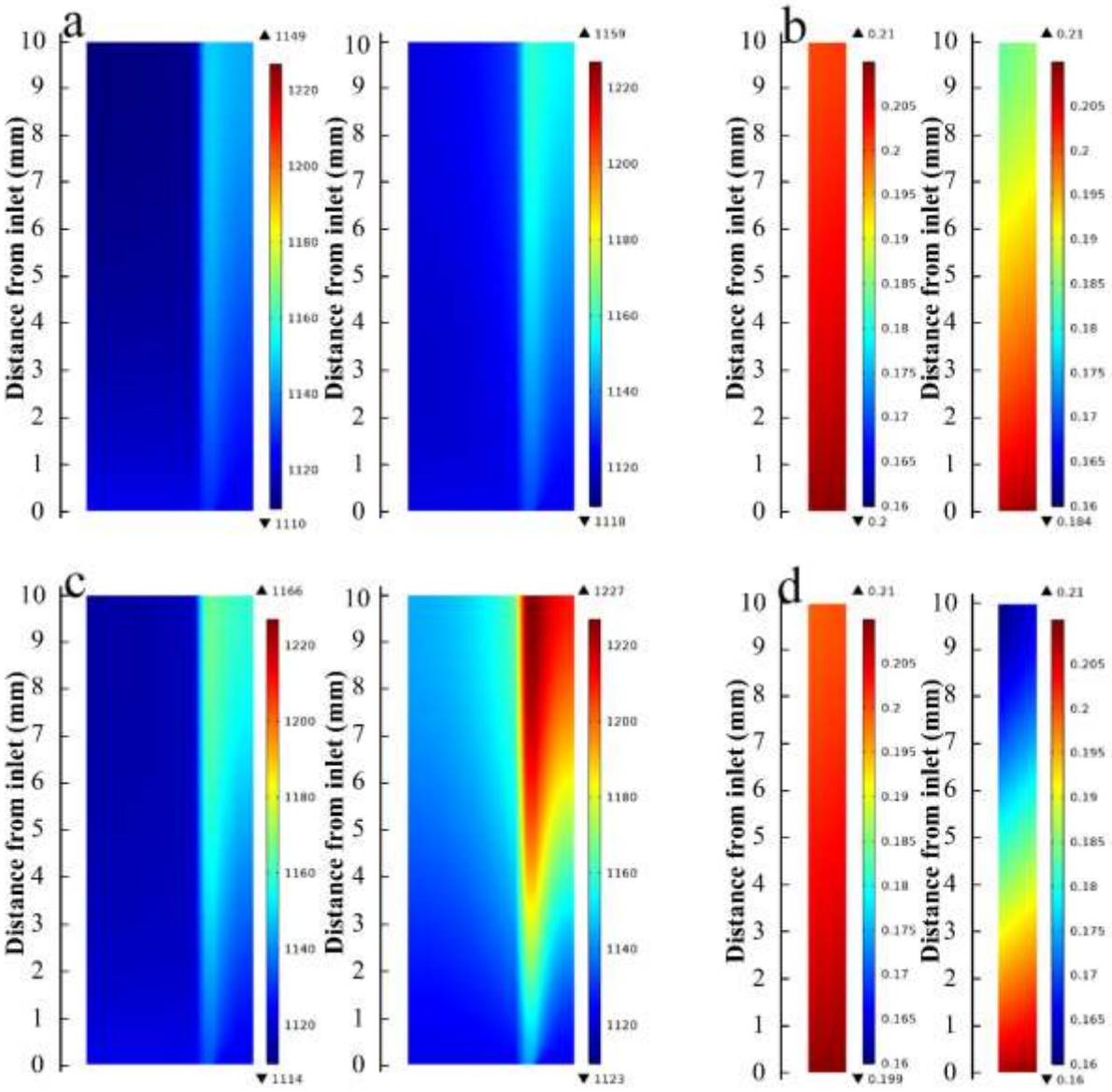

Fig.5 Cell temperature distribution with CO_2 (a) and H_2O (c) as agents and cathode O_2 molar fraction with CO_2 (b) and H_2O (d) as agents at 0.5 V (left) and 0.1 V (right).

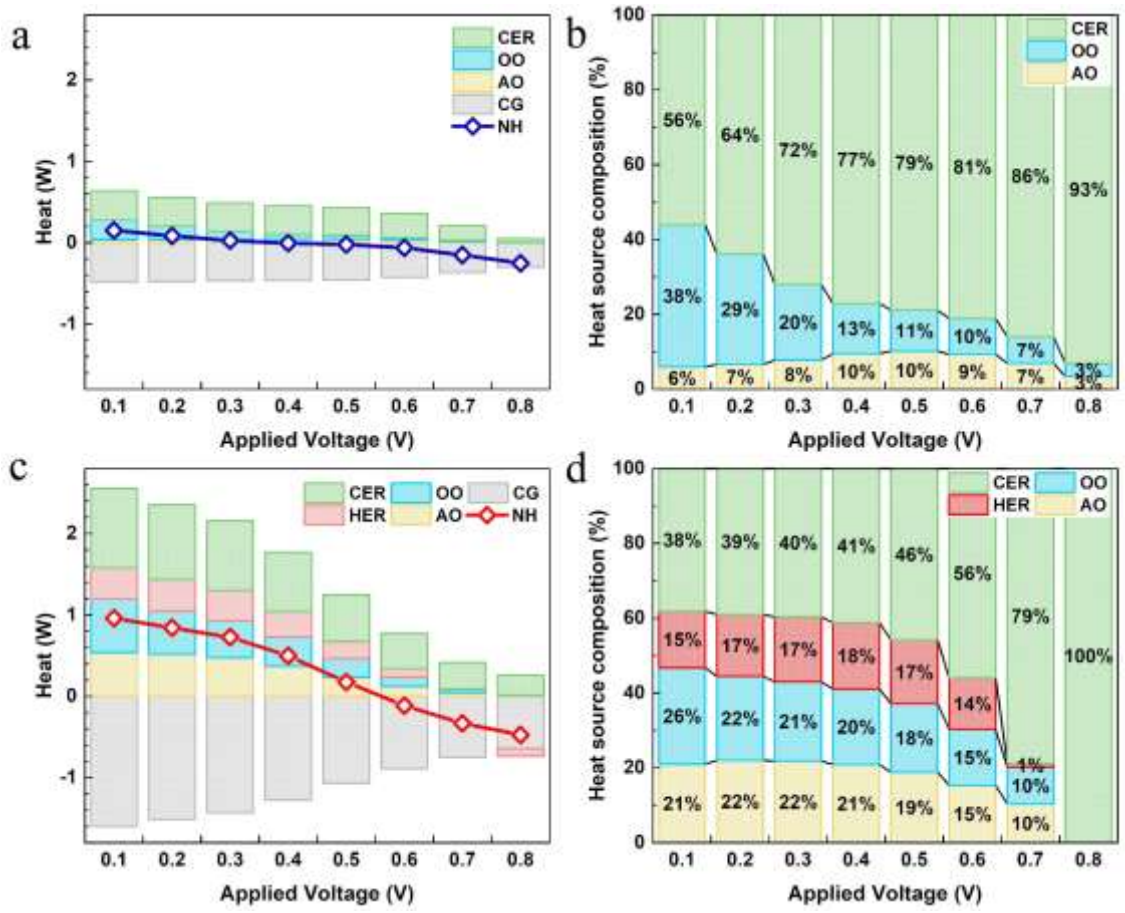

Fig.6 Effects of applied voltage on the heat compositions including CO electrochemical reaction (CER), H_2 electrochemical reaction (HER), ohmic overpotential (OO), activation overpotential (AO) and carbon gasification (CG) and net heat (NH) with CO_2 (a) and H_2O (c) as agents and percentages of different heat sources with CO_2 (b) and H_2O (d) as agents.

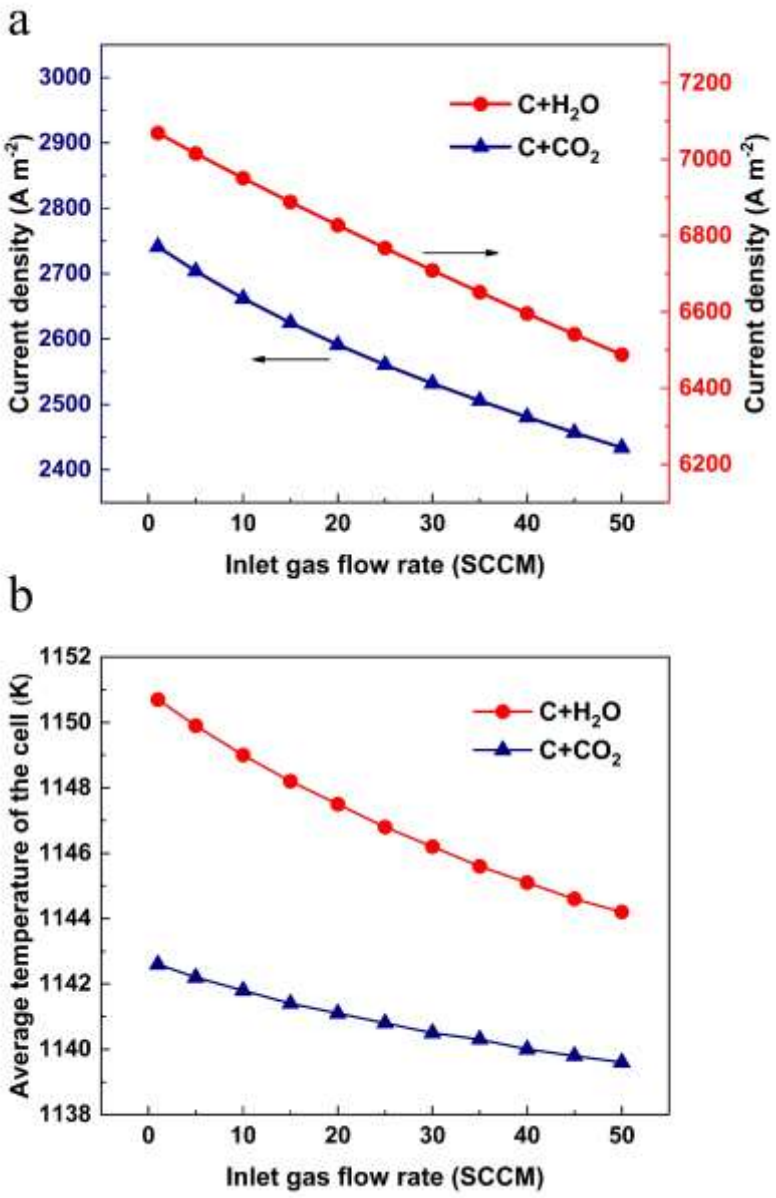

Fig.7 The anode inlet gas flow rate-current (a) and anode inlet gas flow rate-average cell temperature (b) relationships of DC-SOFCs with CO_2 and H_2O as agents.

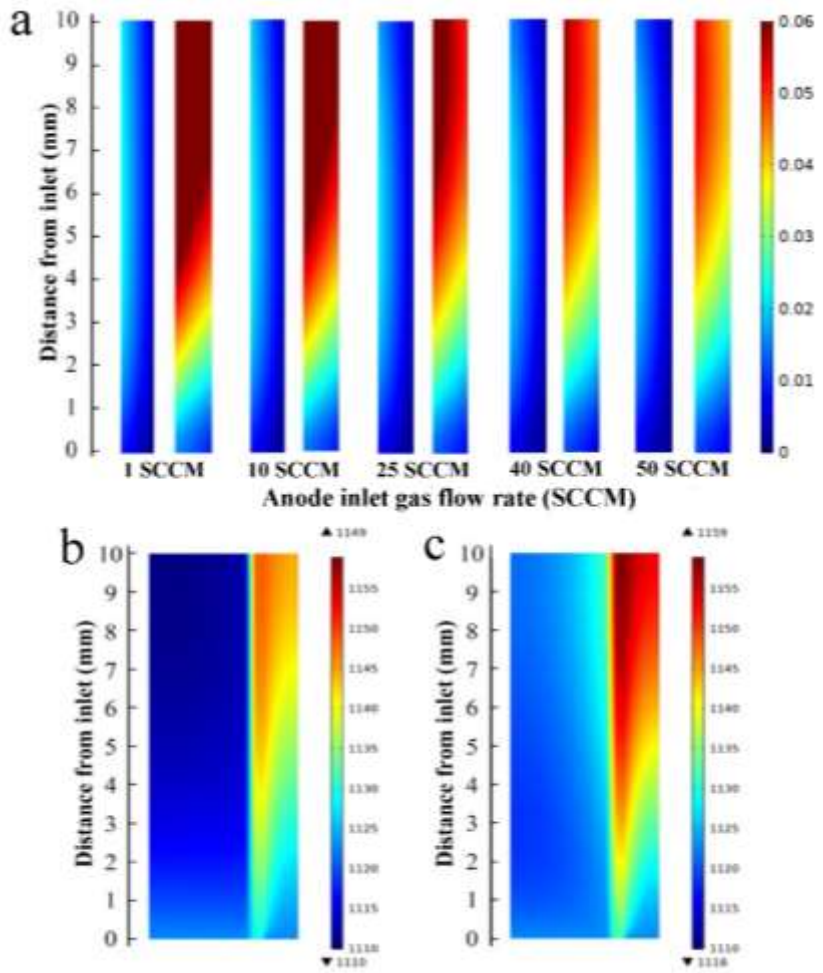

Fig.8 Effects of anode inlet gas flow rate on the fuel gas molar fraction distribution in the anode with CO_2 assisted (left) and H_2O assisted (right) DC-SOFCs at 0.5 V and 1123 K; Cell temperature distribution with CO_2 (b) and H_2O (c) as agents at 10 SCCM anode inlet gas flow rate.

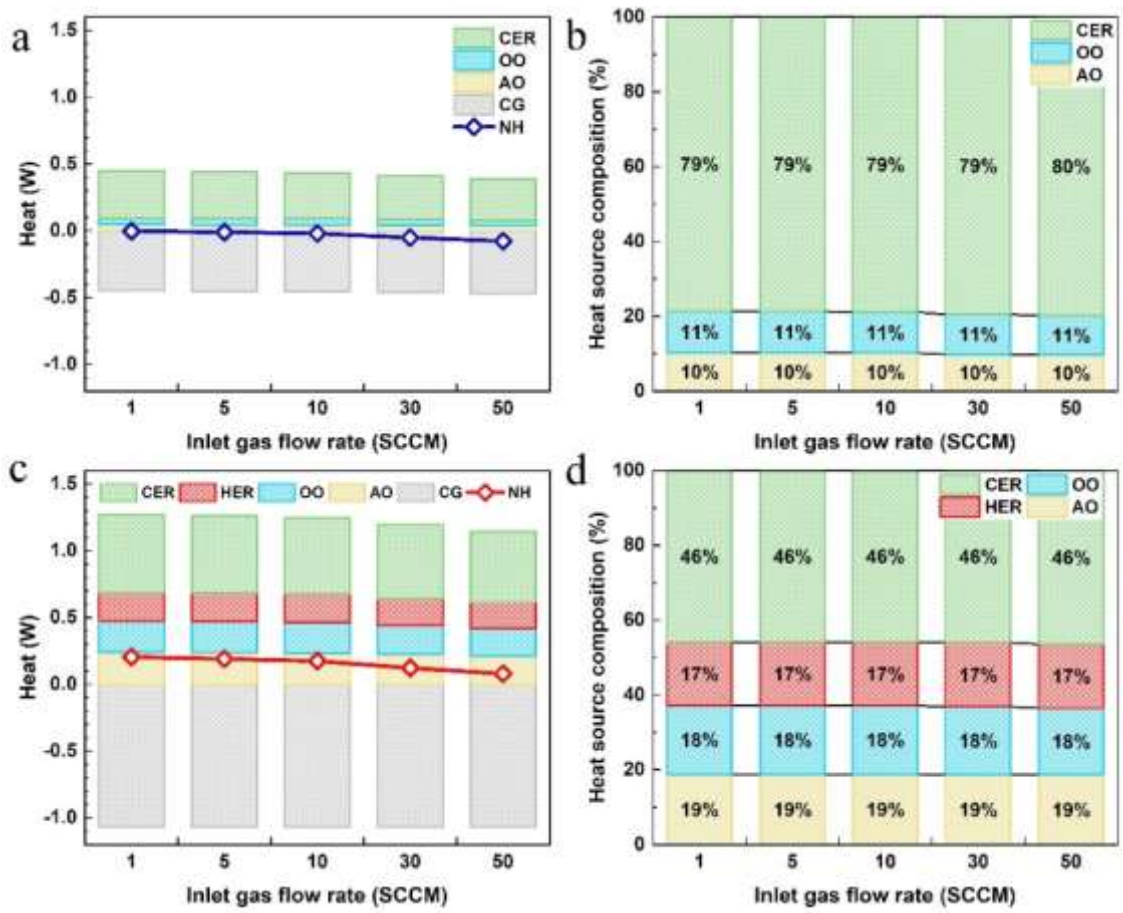

Fig.9 Effects of anode inlet gas flow rate on the heat compositions including CO electrochemical reaction (CER), H_2 electrochemical reaction (HER), ohmic overpotential (OO), activation overpotential (AO) and carbon gasification (CG) and net heat (NH) with CO_2 (a) and H_2O (c) as agents and percentages of different heat sources with CO_2 (b) and H_2O (d) as agents.

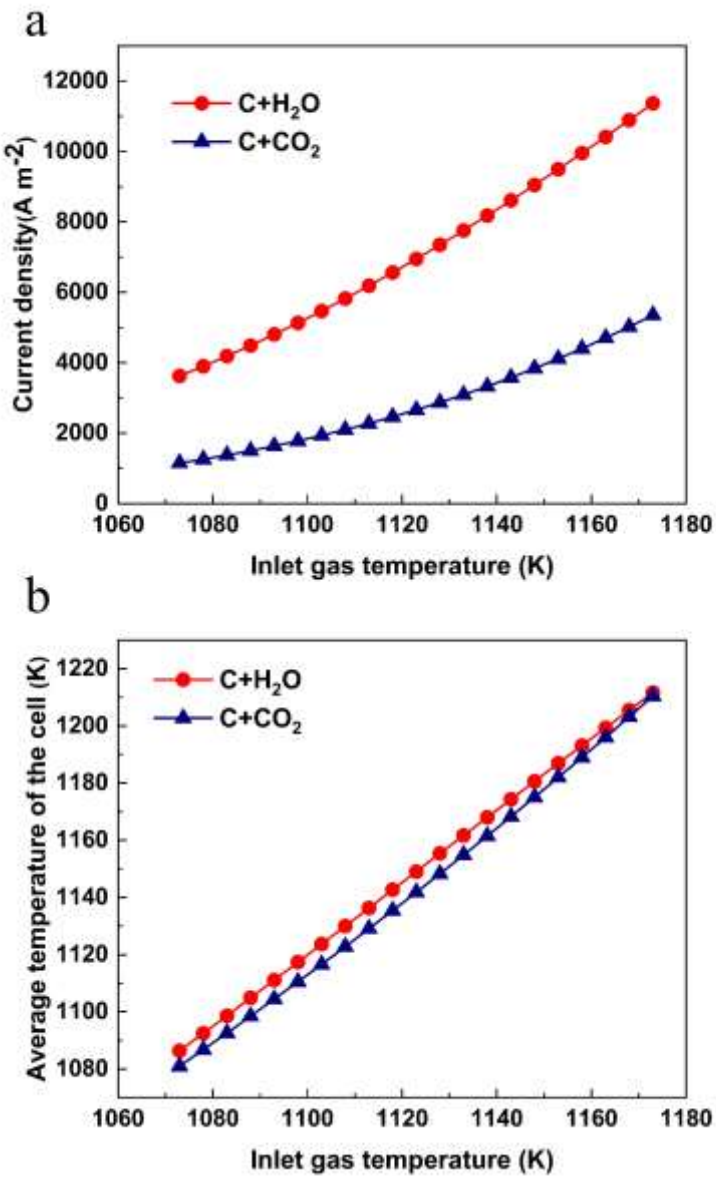

Fig.10 The inlet gas temperature-current (a) and inlet gas temperature-average cell temperature (b) relationships of DC-SOFCs with CO_2 and H_2O as agents.

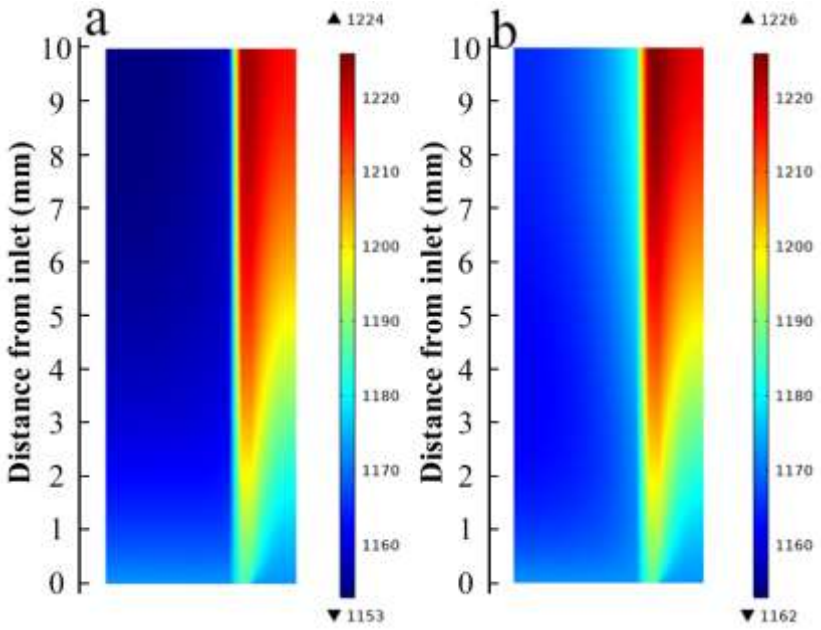

Fig.11 Cell temperature distribution with CO_2 (a) and H_2O (b) as agents at 0.5 V and 1173 K.

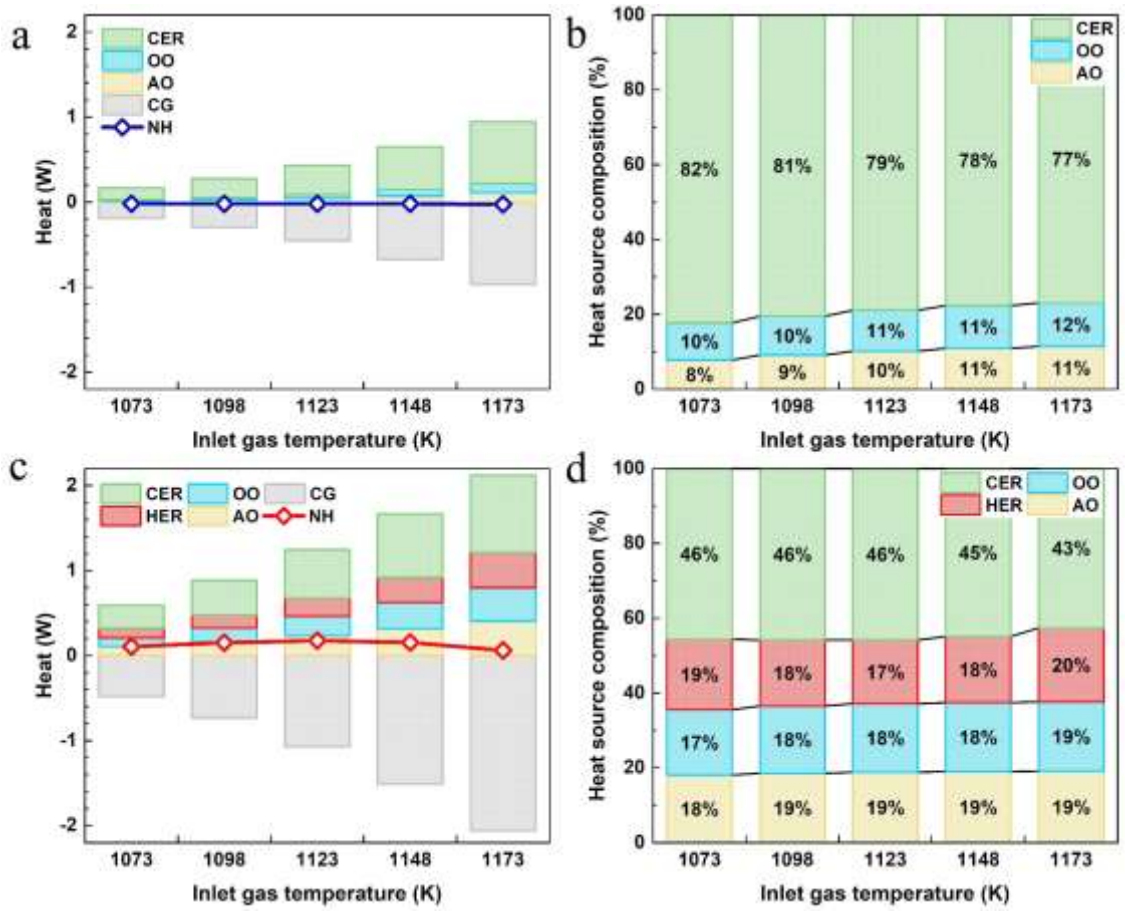

Fig.12 Effects of anode inlet gas flow temperature on the heat compositions including CO electrochemical reaction (CER), H_2 electrochemical reaction (HER), ohmic overpotential (OO), activation overpotential (AO) and carbon gasification (CG) and net heat (NH) with CO_2 (a) and H_2O (c) as agents and percentages of different heat sources with CO_2 (b) and H_2O (d) as agents.

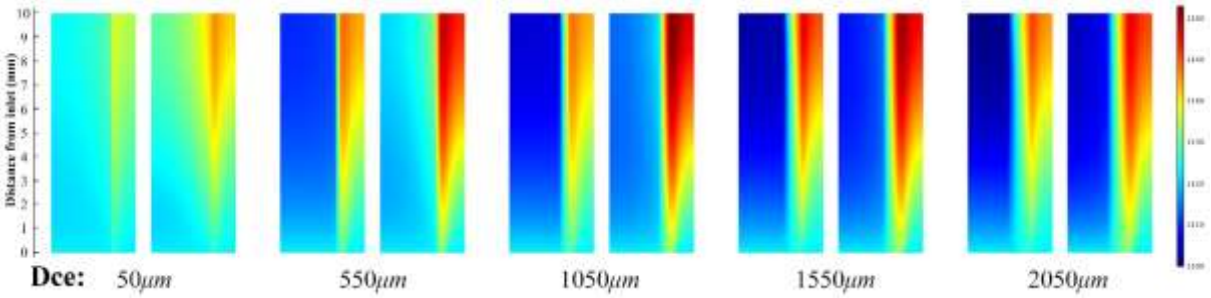

Fig.13 Effects of D_{ce} on the temperature distribution in the cell with CO_2 assisted (left) and H_2O assisted (right) DC-SOFCs at 0.5 V and 1123 K.

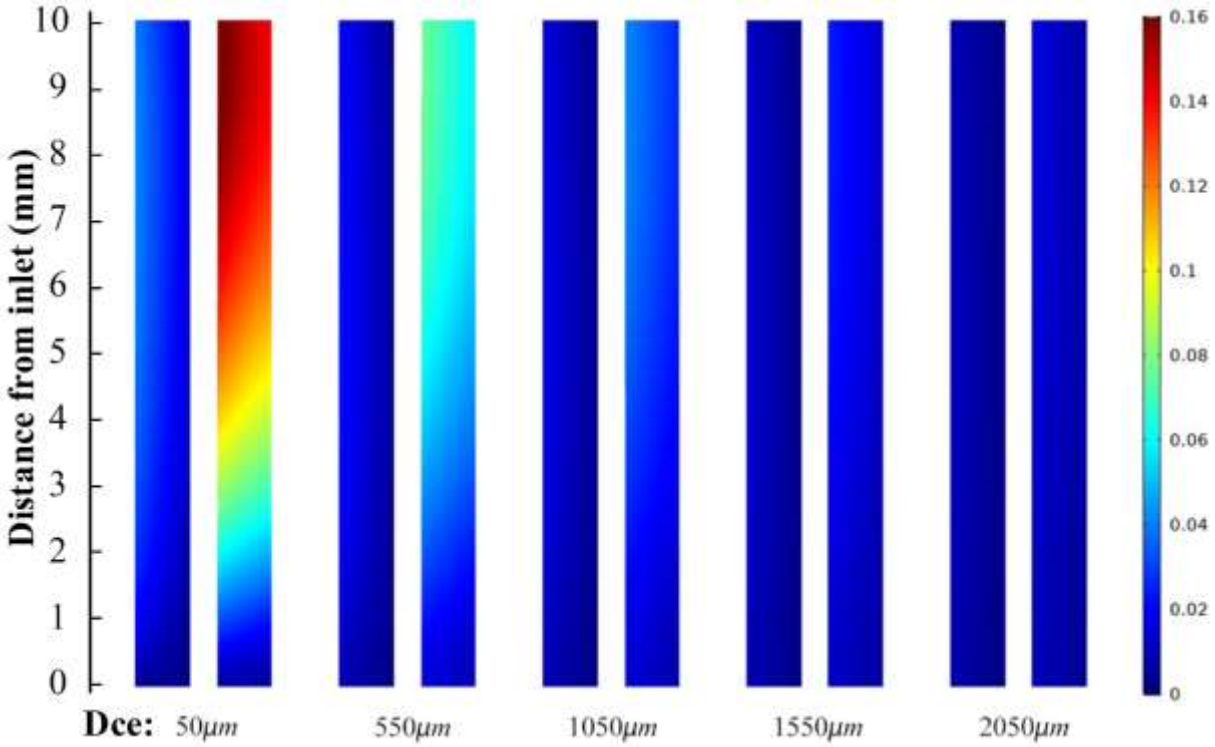

Fig.14 Effects of D_{ce} on the fuel gas molar fraction distribution in the anode with CO_2 assisted (left) and H_2O assisted (right) DC-SOFCs at 0.5 V and 1123 K.

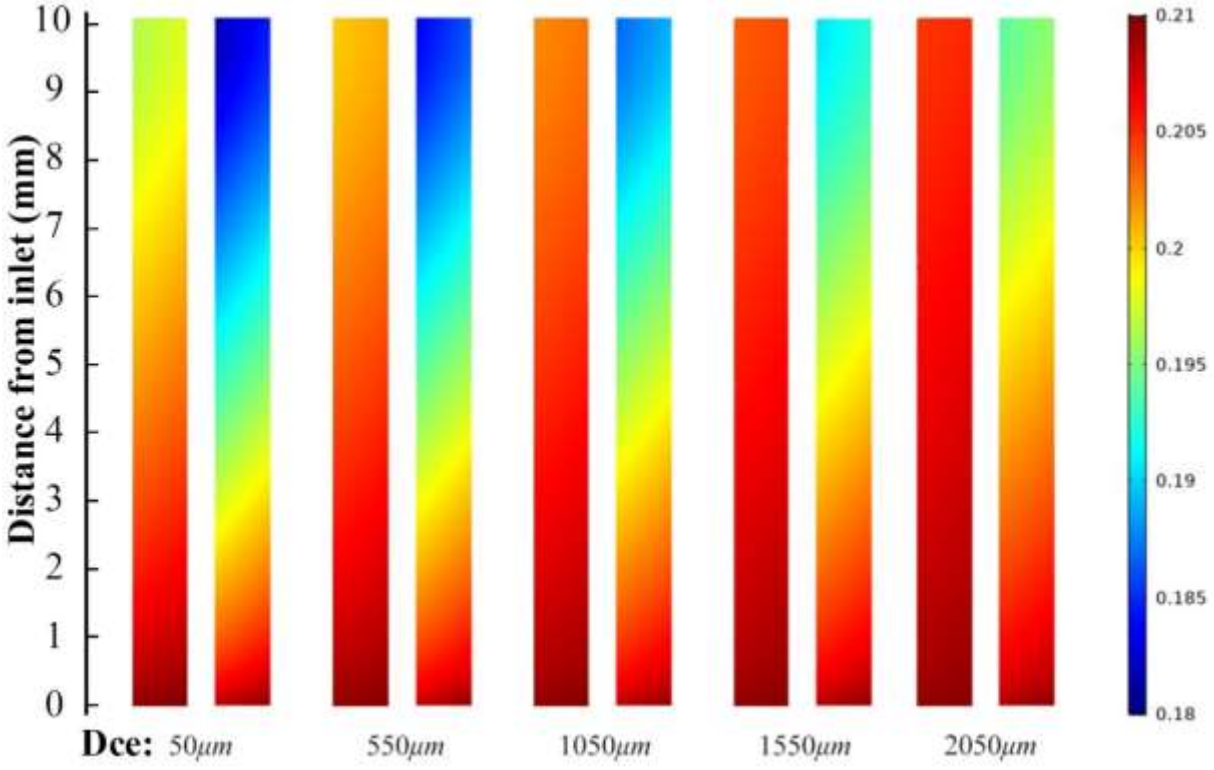

Fig.15 Effects of D_{ce} on the O_2 molar fraction distribution in the cathode with CO_2 assisted (left) and H_2O assisted (right) DC-SOFCs at 0.5 V and 1123 K.

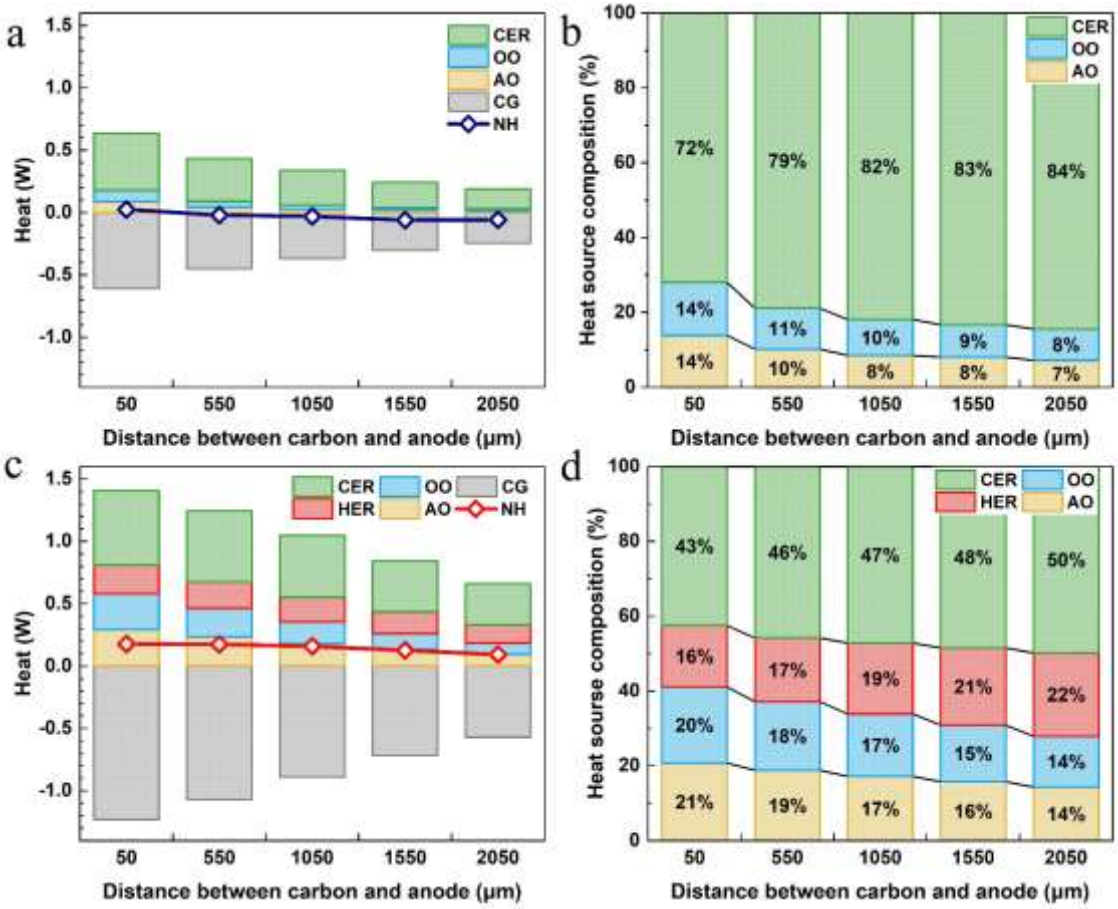

Fig.16 Effects of D_{ce} on the heat compositions including CO electrochemical reaction (CER), H_2 electrochemical reaction (HER), ohmic overpotential (OO), activation overpotential (AO) and carbon gasification (CG) and net heat (NH) with CO_2 (a) and H_2O (c) as agents and percentages of different heat sources with CO_2 (b) and H_2O (d) as agents.